Chromophore selective multi-wavelength photoacoustic remote sensing of unstained human tissues

Saad Abbasi,[1,5] **Martin Le,**[1,5] **Bazil Sonier,**[1] **Kevan Bell,**[1,2] **Deepak Dinakaran,**[2,3] **Gilbert Bigras,**[4] **John R. Mackey,**[3] **and Parsin Haji Reza**[1,*]

[1]*PhotoMedicine Labs, Department of Systems Design Engineering, University of Waterloo, Waterloo, Ontario, N2L 3G1, Canada*

[2]*illumiSonics, Inc., Department of Systems Design Engineering, University of Waterloo, Waterloo, Ontario, N2L 3G1, Canada*

[3]*Department of Oncology, University of Alberta, Edmonton, Alberta, T6G 2V1, Canada*

[4]*Department of Laboratory Medicine and Pathology, University of Alberta, Edmonton, Alberta, T6G 2V1, Canada*

[5]*Equal contributions*

[*]*phajireza@uwaterloo.ca*

Abstract: Identifying positive surgical margins after resection of cancer often triggers re-excision and adjuvant treatments. Incomplete initial resections result in poorer patient outcomes, psychological and financial stress to the patient and increased healthcare costs. Surgical margins are typically assessed post-operatively using time consuming and expensive slide-based histopathology tissue analysis. Currently, a real-time non-contact virtual histology-like intraoperative margin assessment tool is not available. To address this need, we have developed a non-contact multi-wavelength reflection-mode, photoacoustic remote sensing (PARS) microscope demonstrating chromophore selective contrast in human tissues. We show the capabilities of multi-wavelength PARS microscopy utilizing both 266 nm and 532 nm excitation wavelengths and a 1310 nm detection wavelength. Cell nuclei and hemoglobin were visualized at the cellular scale without the addition of exogenous contrast agents. These works provide a critical step towards a virtual histology tool to provide intraoperative histology-like information in living tissue.

1. Introduction

Surgical resection remains one of the most effective primary treatments for most solid cancers [1,2]. The goal of cancer surgery is to remove all cancerous tissue along with a minimal margin of healthy tissue to ensure no cancerous cells remain. To achieve these negative surgical margins, surgical oncologists rely on visual inspection, palpation of tissue, pre-operative imaging and clinical judgement to determine if any cancerous tissue remains. Currently, the gold standard for surgical margin assessment is post-operative histological analysis of resected tissue. Margin assessment is a multi-step process of oriented tissue selection from the resection specimen, production of high-quality histology slides, bright-field microscopic assessment, and integration of the results in three dimensions. To prepare histology slides, tissues must be fixed, sectioned, mounted, and stained. This process requires highly skilled staff, significant resources, and may take up to two weeks to complete. When positive surgical margins are identified, patients frequently require additional surgery for revision of margins, and may need more aggressive adjuvant systemic therapy or radiation therapy. These additional measures impose physical, psychological, and financial burdens on the patient.

Frozen section analysis (FSA) is a commonly used method for intraoperative margin assessment that can reduce re-excision rates and improve patient outcomes in some settings. The accuracy of this process varies widely when compared to standard histopathological sections [3]. FSA requires freezing of the sample that can introduce artifacts in the tissue, reduce the technical quality of the slides and make interpretation difficult [4]. Furthermore, the procedure can take up to an hour to complete, increasing anesthesia and surgical risks [5]. There have been several techniques developed to improve intraoperative assessment and decrease positive margin rates. However, these techniques require the addition of exogenous dyes or optical clearing [6–8]. Photoacoustic (PA) imaging delivers contrast through optical absorption. This enables the targeting of individual endogenous chromophores such as hemoglobin, lipids, cell nuclei, cytochromes, and melanin with specific wavelengths without the addition of any exogenous contrast.

Optical-resolution photoacoustic microscopy has demonstrated visualization of cellular morphology and cytochromes in *ex-vivo* samples [9,10]. However, this technique requires physical contact with the sample to achieve acoustic coupling making it impractical for *in-situ* clinical applications. Physical contact with the surgical site increases the risk of infection, especially as post-operative infections account for 25% of all nosocomial infections [11]. Additionally, use of a contact-based imaging microscope would require extensive sterilization procedures for *in-situ* applications. This method would also require thin samples as it operates in transmission-mode, making it unsuitable for *in-situ* imaging.

A recently reported photoacoustic imaging modality called photoacoustic remote sensing (PARS) microscopy has demonstrated subcellular resolution in a label-free non-contact reflection-mode operation. Unlike conventional PA methods, PARS has demonstrated centimeter-scale working distance, rejecting the requirement of contact-based acoustic coupling [12,13]. Haven *et. al.* have demonstrated PARS' capability in visualizing cultured HeLa cell nuclei and thin slices of HT1080 tumors grown in chicken embryo models by targeting the optical absorption peak of DNA at 266 nm [14]. In this paper, we present the first visualization of cellular morphology in human pancreatic and tonsil tissue samples using a multi-wavelength, label-free, all-optical, non-contact, reflection-mode microscope.

2. Materials and methods

2.1. Sample preparation

Human pancreatic and tonsil tissue samples were obtained under a protocol approved by the Research Ethics Board of Alberta (Protocol ID: HREBA.CC-18-0277) and the University of Waterloo Health Research Ethics Committee (Humans: #40275 Photoacoustic Remote Sensing (PARS) Microscopy of Surgical Resection, Needle Biopsy, and Pathology Specimens). All experiments were performed in accordance with the relevant guidelines and regulations. Specimens of human tissue were attained, with approval of the institutional ethics committee, from clinical collaborators in the Cross-Cancer Institute (Edmonton, Alberta, Canada). These samples were resected and immediately submerged in formaldehyde for fixation, dehydrated, cleared with xylene, infiltrated with hot paraffin wax, and mounted on a cassette. To provide a comparison between PARS images and conventional histopathology images, we prepared a set of hematoxylin and eosin (H&E) stained and adjacent unstained tissue samples. The unstained slides were prepared in the identical manner apart from omitting staining with the H&E dyes. For both the H&E slides and unstained slides, 4 µm thick adjacent sections were cut from the cassettes and placed in a warm water bath, and the sections were transferred to glass sides and baked at 60°C to remove any excess paraffin. The H&E slides were baked for 30 minutes whereas the unstained slides were baked for an hour. Next, the H&E slides were stained with standard H&E staining dyes and covered with a coverslip. The unstained slides were not covered with any coverslips or any other media.

2.2.   Imaging mechanism

PARS utilizes both a pulsed excitation laser and a continuous-wave detection laser in order to generate and detect initial PA pressures. In brief, an excitation pulse incident on an optically absorbing region produces thermo-elastic expansion through the photoacoustic effect generating large initial pressures. These initial pressures modulate the local refractive index via the elasto-optic effect, modulating the scattering properties of this region. Meanwhile, a continuous-wave detection beam is co-focused with the excitation spot. The modulating scattering profile induces intensity variations in the back-scattered detection beam. Photoacoustic signals are measured as variations of this back-scattered intensity. The magnitude of these signals is proportional to the optical absorption of the absorber at the excitation wavelength [12,15,16].

Following the analytical methods described in [12,16], and using values for optical absorption of biomolecules presented by Soltani *et. al.* we calculate the PARS reflectivity changes for cell nuclei to compare against red blood cells (RBC) [17,18]. Cells are modeled using refractive indices of 1.358 and 1.377 for cell nuclei and cytoplasm respectively [19]. Red blood cells are modeled using refractive indices of 1.413 for the cell, and 1.33 for the blood plasma [20,21]. Since both the cell nuclei and the red blood cells are assumed to be much larger than the detection wavelength and the focal spot size, a simple planar interface is assumed. The PARS signal will then be a result of comparing the unperturbed reflection from this structure, assuming a Fresnel interface, and the perturbed reflection following photoacoustic excitation and elasto-optic modulation of the absorbing medium. This signal is then characterized as the reflectivity difference ΔR between these two reflections. This yields reflectivity changes of $\Delta R_{DNA,266} = 1.43 \times 10^{-4}$, $\Delta R_{DNA,532} = 1.88 \times 10^{-7}$, $\Delta R_{RBC,266} = 7.88 \times 10^{-6}$, and $\Delta R_{RBC,532} = 1.78 \times 10^{-5}$ where $\Delta R_{DNA,\lambda}$ is the reflectivity change for DNA in cell nuclei at λ and $\Delta R_{RBC,\lambda}$ is the reflectivity change for RBC at λ. For these calculations excitation fluences are assumed to be at ANSI limits of 3 mJ/cm^2 for 266 nm and 20 mJ/cm^2 for 532 nm. This yields predicted fractional signals of $\Delta R_{DNA,266}/\Delta R_{RBC,266} = 18.1$ at 266 nm and $\Delta R_{RBC,532}/\Delta R_{DNA,532} = 94.5$ at 532 nm.

2.3.   Experimental apparatus

As shown in Fig. 1, a 266 nm 0.5 nanosecond-pulsed laser (SNU-20F-10x, Teem Photonics) operating at 21.4 kHz was filtered through a 25 µm pinhole. The beam was then expanded using a fixed magnification beam expander. This excitation beam was then passed through a dichroic beam combiner where it was combined with a 1310 nm detection source. A 532 nm 3 nanosecond-pulsed laser (VGEN-G-HE-10, Spectra Physics) operating at 20 kHz was expanded by two lenses. It was then fiber coupled using a polarization-maintaining fiber launch (MBT621D, Thorlabs) and a polarization maintaining fiber. The beam was then released from the fiber, passed through a collimator and then expanded using two lenses. The excitation beam was then passed through a dichroic beam combiner (DMLP900R, Thorlabs) where it was combined with a 1310 nm detection source. A 1310 nm superluminescent continuous-wave diode (S5FC1018P, Thorlabs) was fiber coupled and passed through a fiber polarization controller. It was then collimated and expanded using two lenses. The expanded beam was passed through a polarizing beam splitter then was converted into circular polarized light with a zero-order quarter waveplate (WPQ10M-1310, Thorlabs). The beam was then passed through a dichroic beam combiner, where it meets the 532 nm excitation source. The detection beam then passes through another dichroic beam splitter where it meets a 266 nm excitation source. The beams then moved into a 2D galvanometer scanning mirror system and were co-focused and co-scanned using a 0.3 numerical-aperture reflective objective lens (LMM-15x-UVV, Thorlabs). The pulse energies were measured to be 3 nJ and 15 nJ for the 266 nm and 532 nm pulses respectively. The back-reflected detection beam was passed back through the quarter waveplate, converting it from circular polarization to vertical polarization and directed by the polarized beam splitter into a 75 MHz

bandwidth InGaAs balanced photodiode (PDB425C-AC, Thorlabs). During these experiments no thermal damage to the samples was observed during the study.
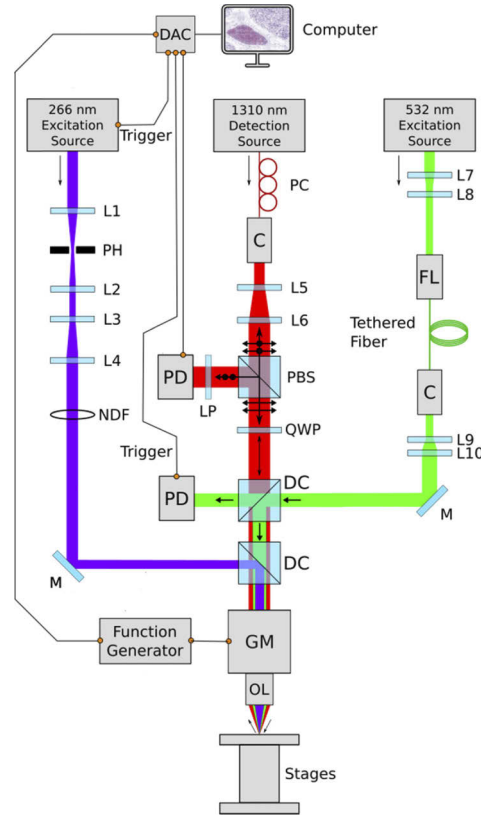
Fig. 1. Simplified schematic of multi-wavelength PARS microscope. Components labels are defined as: pinhole (PH), neutral density filter (NDF), collimator (C), polarized beam splitter (PBS), quarter waveplate (QWP), dichroic mirror (DC), photodiode (PD), fiber launch (FL), galvanometer mirrors (GM), objective lens (OL), mirror (M)

2.4. Image formation

High resolution small field of view acquisitions were acquired using a 2D galvanometer mirror system to direct the beam. A raster-like scan pattern was created using a function generator which produced two ramp waveforms with fixed frequencies of 30 Hz and 60 mHz. Positional signals from the 2D galvanometer mirror system and the mechanical stages were recorded using a 16-bit data acquisition card (CSE161G4, Gage Applied). The PARS modulation event produced a voltage signal from the balanced photodiode and was also recorded using the digitizer card. A Hilbert transform was applied to the raw time domain signals and the absolute values of the functions were extracted. Images were then formed by taking a maximum amplitude projection of each modulation event and were Delaunay interpolated to fit in a Cartesian grid. A greyscale colour map was applied to the images. Mosaic images were formed by capturing successive high-resolution small field of view acquisitions in a grid pattern. In-house developed software allowed for precision movement of the linear translation stages after each high-resolution acquisition. Each mosaic image was 100 μm x 100 μm in size and took four seconds to acquire at a laser repetition rate of 20 kHz. Mosaic sections were stitched together using ImageJ's Grid/Collection Stitching Plugin [22], which determines optimal positioning of the sections

using a cross-correlation algorithm. A color map was then applied to the respective 266 nm and 532 nm acquisitions to simulate an H&E-stained histology-like image.

2.5. Resolution characterization

To characterize the lateral resolution of the system, carbon fibers were imaged at 266 nm (Fig. 2(a)) and 532 nm (Fig. 2(c)) wavelengths. The resolution is characterized by fitting an edge spread function to a carbon fiber's edge pixel values. The lateral resolution is then defined as the width between the 10% and 90% of the edge spread function. The resolution for the 266 nm beam was found to be 1.2 μm and for 532 nm was found to be 1.5 μm.
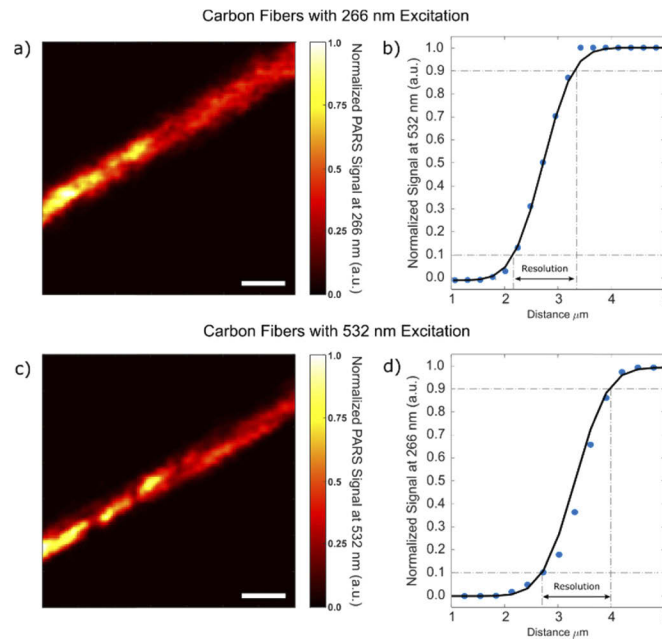
Fig. 2. Resolution characterization of the multi-wavelength PARS system **(a)** carbon fibers imaged with the 266 nm excitation **(b)** corresponding edge-spread function measuring a resolution of 1.2 μm **(c)** carbon fibers imaged with the 532 nm excitation **(d)** corresponding edge spread function measuring a resolution of 1.5 μm. Scale bar 10 μm.

3. Results and discussion

Figure 3 compares a high-resolution H&E image (Fig. 3(a)) of human epidermal tissue with a PARS image (Fig. 3(b)) of an unstained adjacent section. The PARS image is able to resolve cell nuclei similar to the H&E section. As the images are of adjacent sections and not of the same tissue sample, the cell nuclei do not appear at the same locations in both images.

Using the apparatus described in Fig. 1, we imaged and compared unstained human pancreatic (Fig. 4) and tonsil tissue (Fig. 5) sections to adjacent H&E stained sections (Fig. 4(a) and Fig. 5(a)). The tissue sections were first imaged with a 266 nm excitation wavelength (Fig. 4(b) and Fig. 5(b)) followed by a 532 nm excitation wavelength (Fig. 4(c) and Fig. 5(c)). The 266 nm and 532 nm images were then superimposed as shown in Fig. 4(d) and Fig. 5(d) emulating contrast from an H&E colour map.

The contrast provided in Fig. 4(b) and Fig. 5(b) image highlights the optical absorption of DNA at 266 nm. As a result, cellular morphology and bulk tissue structure is distinguishable in reference to the H&E prepared section. The areas corresponding to hemoglobin (blue outlines in
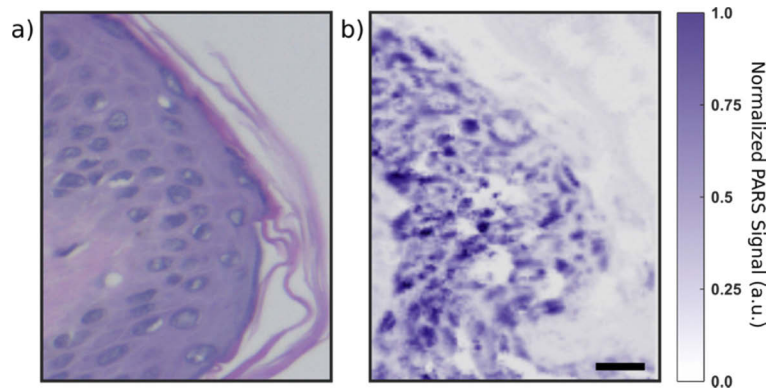
Fig. 3. **(a)** high-resolution H&E image of human epidermal tissue **(b)** high-resolution PARS image with a 266 nm excitation of an adjacent section. Color bar represents normalized PARS signal. Scale bar 10 μm.
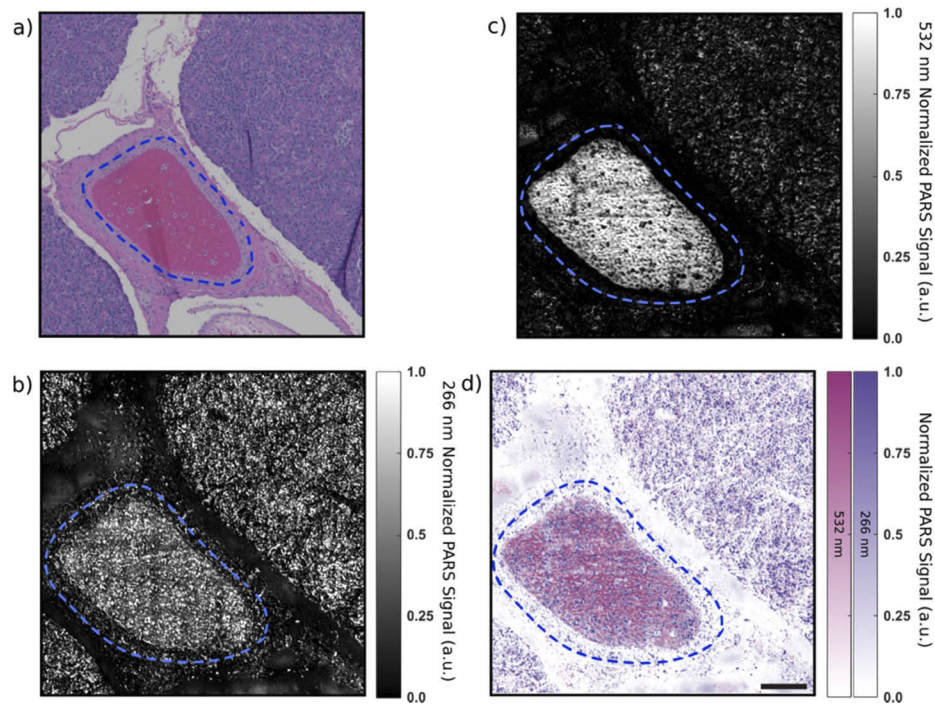
Fig. 4. **(a)** A standard H&E stained slide of a blood vessel (blue outline) within human pancreatic tissue imaged with a conventional brightfield microscope. **(b)** An adjacent unstained slide of the same specimen imaged with 266 nm excitation and **(c)** with 532 nm excitation. **(d)** A superimposed image of **(b)** and **(c)** with a histology-like colormap, DNA is colored purple, hemoglobin is colored red. Scale bar 100 μm.

Fig. 4 and Fig. 5) lack signal in the cells presumed to be erythrocytes, since they are anuclear and do not have DNA to strongly absorb the 266 nm excitation. Similarly, 532 nm excitation images shown in Fig. 4(c) and Fig. 5(c) presents hemoglobin contrast as comparable to their corresponding H&E prepared section. The blood vessel as outlined in Fig. 4(d) can be identified in comparison to the H&E prepared section in Fig. 4(a). The 266 nm signal (Fig. 4(b)) also shows
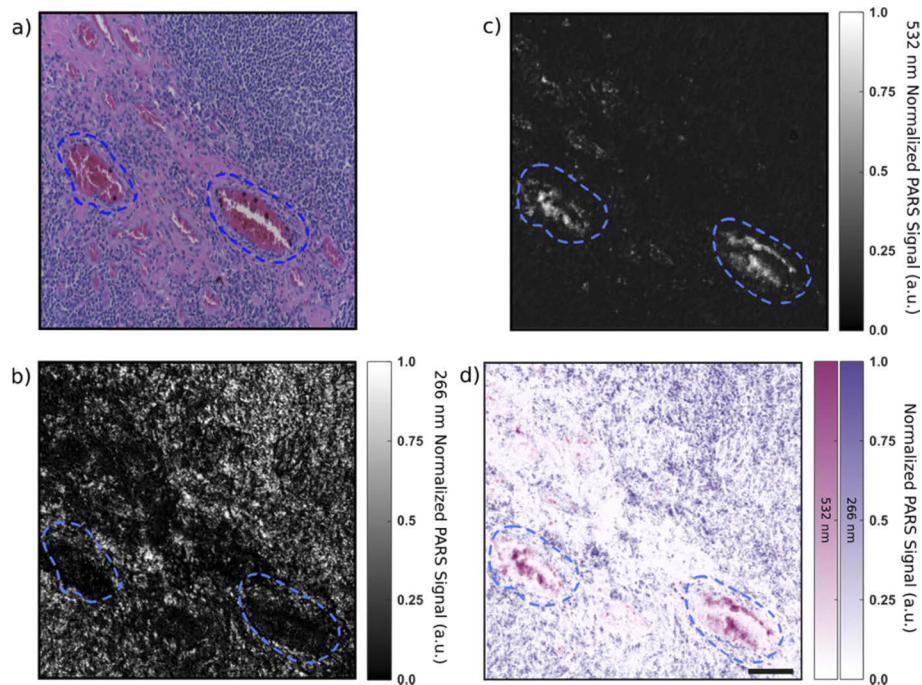
Fig. 5. **(a)** A standard H&E stained slide of venules (blue outline) embedded within a human tonsil tissue imaged with a conventional brightfield microscope. **(b)** An adjacent unstained slide of the same specimen imaged with 266 nm excitation and **(c)** with 532 nm excitation. **(d)** A superimposed image of **(b)** and **(c)** with a histology-like colormap, DNA is colored purple, hemoglobin is colored red. Scale bar 100 μm.

other nucleated cells of blood in the vessel lumen, such as leukocytes, that are clearly evident in the background of the 532 nm signal from erythrocytes (Fig. 4(c)). The PARS-imaged signals from erythrocytes and nucleated cells of blood correspond well with the H&E image (Fig. 4(a)), and (Fig. 4(d)) suggest an enhanced ability of PARS to identify these nucleated cells amongst the population of erythrocytes. Similarly, the hemoglobin highlighted by the 532 nm excitation (Fig. 5(c)) in the tonsil tissue is comparable to the location of erythrocytes in Fig. 5(a). Although hemoglobin and DNA are assumed to be the primary absorbers at the excitation wavelengths, other chromophores such as cytochrome and collagen will produce non-zero signals at these same wavelengths. However, their contributions are considered to be negligible.

Nuclear density, morphology, and organization are critical identifiers which are commonly used to diagnose tissue samples. For example, the nucleus is the best cellular sub-unit to identify a cell. Semi-quantitative measurements such as the "nucleus/cytoplasm" ratio (N/C) are used in order to identify malignant versus healthy cells, as malignant cells are biologically more aggressive and therefore tend to have a larger nucleus and smaller cytoplasm. As we demonstrate PARS is capable of imaging targeted chromophores in human tissues with a multi-wavelength excitation design, additional excitation wavelengths may be added to image additional chromophores. A 422 nm excitation wavelength has previously shown efficacious visualization of the cytoplasm, emulating an eosin-like stain [10]. Furthermore, a 1197 nm excitation wavelength has been previously used to image adipose tissue which is otherwise lost during the extensive H&E staining process [23]. These features can be useful in distinguishing among different tissue types and are some of the important histopathologic features that distinguish normal tissue from cancerous tissue. The contrast delivered by multi-wavelength excitation PARS permits regions of cancer to

be identified even if they are macroscopically indistinguishable from benign tissue, which can guide more accurate surgical resection.

4. Conclusion

This work represents the first report of a non-contact multi-wavelength microscope capable of label-free visualization of cellular morphology and hemoglobin. Unstained slides of human pancreas and tonsil tissue samples were imaged and were found to be comparable to conventional H&E processed slides, highlighting cellular morphology and hemoglobin. The addition of hemoglobin presents a vital step towards clinically useful *in-situ* histology-like imaging. Furthermore, this report demonstrates PARS' ability to incorporate additional excitation wavelengths to selectively deliver label-free contrast for various components of tissue structure such as cytochrome, lipids or adipocytes, potentially enabling microscopic intraoperative assessment of living tissue.

Funding

Disclosures

DD, KB, JRM and PHR have financial interests in illumiSonics Inc. IllumiSonics partly supported this work.

References

1. J. M. Kurtz, R. Amalric, H. Brandone, Y. Ayme, J. Jacquemier, J.-C. Pietra, D. Hans, J.-F. Pollet, C. Bressac, and J.-M. Spitalier, "Local recurrence after breast-conserving surgery and radiotherapy. Frequency, time course, and prognosis," Cancer **63**(10), 1912–1917 (1989).
2. N. Martini, M. S. Bains, M. E. Burt, M. F. Zakowski, P. McCormack, V. W. Rusch, and R. J. Ginsberg, "Incidence of local recurrence and second primary tumors in resected stage I lung cancer," J. Thorac. Cardiovasc. Surg. **109**(1), 120–129 (1995).
3. S. R. Shi, C. Liu, L. Pootrakul, L. Tang, A. Young, R. Chen, R. J. Cote, and C. R. Taylor, "Evaluation of the value of frozen tissue section used as "gold standard" for immunohistochemistry," Am. J. Clin. Pathol. **129**(3), 358–366 (2008).
4. E. B. Desciak and M. E. Maloney, "Artifacts in frozen section preparation," Dermatol. Surg. **26**(5), 500–504 (2000).
5. G. M. Bricca, D. G. Brodland, and J. A. Zitelli, "Immunostaining Melanoma Frozen Sections: The 1-Hour Protocol," Dermatol. Surg. **30**(3), 403–408 (2004).
6. E. A. te Velde, T. Veerman, V. Subramaniam, and T. Ruers, "The use of fluorescent dyes and probes in surgical oncology," Eur. J. Surg. Oncol. **36**(1), 6–15 (2010).
7. D. Zhu, K. V. Larin, Q. Luo, and V. V. Tuchin, "Recent progress in tissue optical clearing," Laser Photonics Rev. **7**(5), 732–757 (2013).
8. A. M. Zysk, K. Chen, E. Gabrielson, L. Tafra, E. A. May Gonzalez, J. K. Canner, E. B. Schneider, A. J. Cittadine, P. Scott Carney, S. A. Boppart, K. Tsuchiya, K. Sawyer, and L. K. Jacobs, "Intraoperative Assessment of Final Margins with a Handheld Optical Imaging Probe During Breast-Conserving Surgery May Reduce the Reoperation Rate: Results of a Multicenter Study," Ann. Surg. Oncol. **22**(10), 3356–3362 (2015).
9. T. T. W. Wong, R. Zhang, P. Hai, C. Zhang, M. A. Pleitez, R. L. Aft, D. V. Novack, and L. V. Wang, "Fast label-free multilayered histology-like imaging of human breast cancer by photoacoustic microscopy," Sci. Adv. **3**(5), e1602168 (2017).
10. C. Zhang, Y. S. Zhang, D.-K. Yao, Y. Xia, and L. V. Wang, "Label-free photoacoustic microscopy of cytochromes," J. Biomed. Opt. **18**(2), 020504 (2013).
11. R. L. Nichols, "Preventing surgical site infections: A surgeon's perspective," Emerg. Infect Dis. **7**(2), 220–224 (2001).
12. P. Hajireza, W. Shi, K. Bell, R. J. Paproski, and R. J. Zemp, "Non-interferometric photoacoustic remote sensing microscopy," Light: Sci. Appl. **6**(6), e16278 (2017).
13. P. H. Reza, K. Bell, W. Shi, J. Shapiro, and R. J. Zemp, "Deep non-contact photoacoustic initial pressure imaging," Optica **5**(7), 814–820 (2018).

14. N. J. M. Haven, K. L. Bell, P. Kedarisetti, J. D. Lewis, and R. J. Zemp, "Ultraviolet photoacoustic remote sensing microscopy," Opt. Lett. **44**(14), 3586–3589 (2019).

15. K. L. Bell, P. Hajireza, W. Shi, and R. J. Zemp, "Temporal evolution of low-coherence reflectrometry signals in photoacoustic remote sensing microscopy," Appl. Opt. **56**(18), 5172–5181 (2017).

16. K. Bell, P. Hajireza, and R. Zemp, "Scattering cross-sectional modulation in photoacoustic remote sensing microscopy," Opt. Lett. **43**(1), 146–149 (2018).

17. S. Soltani, A. Ojaghi, and F. E. Robles, "Deep UV dispersion and absorption spectroscopy of biomolecules," Biomed. Opt. Express **10**(2), 487–499 (2019).

18. J. McHowat, J. H. Jones, and M. H. Creer, "Quantitation of individual phospholipid molecular species by UV absorption measurements," J. Lipid Res. **37**, 2450–2460 (1996).

19. M. Schürmann, J. Scholze, P. Müller, J. Guck, and C. J. Chan, "Cell nuclei have lower refractive index and mass density than cytoplasm," J. Biophotonics **9**(10), 1068–1076 (2016).

20. G. S. Adair and M. E. Robinson, "The specific refraction increments of serum-albumin and serum-globulin," Biochem. J. **24**(4), 993–1011 (1930).

21. J. Vörös, "The density and refractive index of adsorbing protein layers," Biophys. J. **87**(1), 553–561 (2004).

22. S. Preibisch, S. Saalfeld, and P. Tomancak, "Globally optimal stitching of tiled 3D microscopic image acquisitions," Bioinformatics **25**(11), 1463–1465 (2009).

23. R. Li, M. N. Slipchenko, P. Wang, and J.-X. Cheng, "Compact high power barium nitrite crystal-based Raman laser at 1197 nm for photoacoustic imaging of fat," J. Biomed. Opt. **18**(4), 040502 (2013).